analytical chemistry

pubs.acs.org/ac Article

Rapid Point-of-Care COVID-19 Diagnosis with a Gold-Nanoarchitecture-Assisted Laser-Scribed Graphene Biosensor

Tutku Beduk, Duygu Beduk, José Ilton de Oliveira Filho, Figen Zihnioglu, Candan Cicek, Ruchan Sertoz, Bilgin Arda, Tuncay Goksel, Kutsal Turhan, Khaled N. Salama,* and Suna Timur*

Cite This: https://doi.org/10.1021/acs.analchem.1c01444 Read Online

ACCESS | Metrics & More | Article Recommendations | Supporting Information

ABSTRACT: The global pandemic caused by the severe acute respiratory syndrome coronavirus 2 (SARS-CoV-2) virus has revealed the urgent need for accurate, rapid, and affordable diagnostic tests for epidemic understanding and management by monitoring the population worldwide. Though current diagnostic methods including real-time polymerase chain reaction (RT-PCR) provide sensitive detection of SARS-CoV-2, they require relatively long processing time, equipped laboratory facilities, and highly skilled personnel. Laser-scribed graphene (LSG)-based biosensing platforms have gained enormous attention as miniaturized electrochemical systems, holding an enormous potential as point-of-care (POC) diagnostic tools. We describe here a miniaturized LSG-based electrochemical sensing scheme for coronavirus disease 2019 (COVID-19) diagnosis combined with three-dimensional (3D) gold nanostructures. This electrode was modified with the SARS-CoV-2 spike protein antibody following the proper surface modifications proved by X-ray photoelectron spectroscopy (XPS) and scanning electron microscopy (SEM) characterizations as well as electrochemical techniques. The system was integrated into a handheld POC detection system operated using a custom smartphone application, providing a user-friendly diagnostic platform due to its ease of operation, accessibility, and systematic data management. The analytical features of the electrochemical immunoassay were evaluated using the standard solution of S-protein in the range of 5.0−500 ng/mL with a detection limit of 2.9 ng/mL. A clinical study was carried out on 23 patient blood serum samples with successful COVID-19 diagnosis, compared to the commercial RT-PCR, antibody blood test, and enzyme-linked immunosorbent assay (ELISA) IgG and IgA test results. Our test provides faster results compared to commercial diagnostic tools and offers a promising alternative solution for next-generation POC applications.

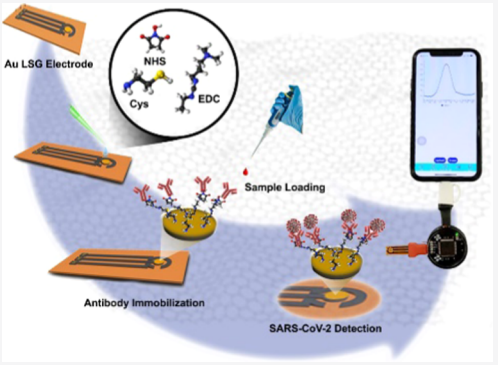

INTRODUCTION

Coronavirus 2 (SARS-CoV-2) causes a severe acute respiratory syndrome commonly known as coronavirus disease (COVID-19).[1,2] The disease was first reported in January 2020 in Wuhan, China, and officially announced as a pandemic by the World Health Organization (WHO) in March 2020.[3] This single-stranded RNA virus attaches to the host cell surface receptor by transmembrane spike glycoproteins.[1] This binding is achieved by the S1 and S2 subunits of the spike protein between viral and cellular membranes.[4,5] Recently, researchers have focused on developing rapid detection systems using both subunits since the monitoring and managing of the pandemic are extremely critical. The most widely used current diagnostic method, real-time polymerase chain reaction (RT-PCR) testing, is the gold standard and the most accessible diagnostic tool for SARS-CoV-2 identification.[6,7]

Other methods are based on the detection of immunoglobulins such as IgM and/or IgG.[8,9] Examples include the enzyme-linked immunosorbent assay (ELISA), lateral flow immunoassays (LFIs), real-time loop-mediated isothermal amplification (RT-LAMP), or CRISPR-Cas9-linked RT-LAMP technologies.[10−14] Detection of IgG and IgM antibodies is related to the identification of SARS-CoV-2 around 10 days after the first symptoms.[15,16] Though these tests provide important immunological evidence, they often require expensive equipment and laboratory conditions.[17,18] Moreover, the cross-reactivity of co-existing biological markers may lead to false-positive results. Thus, oftentimes, patient samples with positive results require further confirmation with alternative testing methods.[19] Developing effective, cheap, and rapid detection kits helps infected cases to be confirmed by allowing individuals to carry out the tests without a need for expertise to save time and resources. Other than clinical diagnostic techniques, point-of-care (POC) diagnostic systems could pave the way and start a new era for the screening of viruses.[20]

Received: April 6, 2021
Accepted: May 20, 2021

Several methods and devices have been proposed using materials extracted from body fluids.[21] Recently, researchers found that volatile organic compounds (VOCs) could emerge in exhaled breath in the early stages of the infection, enabling COVID-19 detection.[22] Electrochemical biosensors have been widely used by researchers as monitoring tools for disease detection. However, various types of biosensing platforms based on electrochemical strategies for COVID-19 diagnosis are yet to be explored. Fabiani et al. developed an electrochemical immunoassay using screen-printed electrodes with an immunological label for COVID-19 diagnosis from saliva samples.[23] Yakoh et al. developed a paper-based immunosensor based on electrochemical detection from real clinical patient sera.[24] Furthermore, Seo et al. reported a biosensing platform based on a field-effect transistor (FET) for COVID-19 diagnosis in clinical samples, leading to very low detection limits.[25] However, despite the various advantages of reported immunoassays, such as sensitivity and accuracy, they require complex and expensive equipment and time-consuming sample pretreatments. Previously used metal electrodes such as Pt and Au are costly and require lithography or masks for the fabrication compared to carbon-based materials that can be easily and cheaply produced by various methods without a need for masks.[26] Therefore, graphene-based materials can be more accessible for the production of diagnostic kits for in-field testing as an urgent need for controlling the spread of highly contagious COVID-19.

Graphene is an extremely conductive and stable material with high surface area.[27] However, due to the absence of chemically reactive functional groups of graphene, the surface may require further nanoparticle functionalization. Nanoparticles have been widely used in healthcare applications, thanks to their ability to increase catalytic activity and deactivate bacteria, viruses, and fungi photothermally or by generating reactive oxygen species.[28] The graphene surface has the ability to adsorb guest molecules conveniently, leading to high sensitivity for various sensing applications.[27,29−31] Since most of the graphene production methods are widely known as expensive and time consuming, laser scribing of polyimide (PI) sheets is a straightforward and mask-free graphene production method. This technique provides graphene multilayers with large surface area and low amount of defects due to the atomic rearrangement on the surface and the formation of stacked graphene flakes, high level of electronic state density, and high electrocatalytic activity.[32,33] Various laser-scribed sensing platforms have been reported previously for biomarker detection.[34−39]

We describe here a method for the quantification of SARS-CoV-2 levels in blood serum by recognizing its protein host cell receptor domain. It makes use of laser-scribed graphene (LSG) and electrodeposited gold nanostructures (AuNSs) in a disposable electrochemical immunoassay. For this purpose, a gold-modified LSG surface was modified with cysteamine and 1-ethyl-3-(3-dimethylaminopropyl) carbodiimide:*N*-hydroxy succinimide (EDC:NHS) as a cross-linking agent to create electroactive groups on the surface. Finally, the system was integrated into a POC system with a smartphone attachment, enabling the diagnostic system to evolve into a portable, easy-to-use, and reliable diagnostic tool for the SARS-CoV-2 virus. The system is considered as affordable since it is based on cheap graphene material and requires only 1 h incubation time. Thus, patients have the possibility to test themselves and take necessary actions, such as self-isolation.[40] A clinical study was carried out to evaluate the accuracy and applicability of the system. The assay was applied to both a buffer solution and the blood serum samples collected from COVID-19 patients, compared to the clinically approved methods.

METHODS

Materials and Apparatus. Cysteamine hydrochloride, 1-ethyl-3-(3-dimethylaminopropyl) carbodiimide (EDC), *N*-hydroxy succinimide (NHS), gold(III) chloride hydrate ($HAuCl_4$), hydrochloric acid (HCl), and bovine serum albumin (BSA) (lyophilized powder, ≥96% (agarose gel electrophoresis)) were purchased from Sigma-Aldrich (St. Louis, MO). Potassium chloride (KCl), potassium ferricyanide ($K_3[Fe(CN)_6]$), and potassium ferrocyanide ($K_4[Fe(CN)_6]$) were purchased from MP Biomedicals. The phosphate-buffered saline (PBS) tablets containing 0.0027 M potassium chloride (KCl) and 0.137 M sodium chloride (NaCl) with pH 7.4 were purchased from Fisher Bioreagents. Differential pulse voltammetry (DPV) and cyclic voltammetry (CV) were carried out using a PalmSens potentiostat (Palm Instruments, Houten, the Netherlands). Immunoglobulin M (IgM) (cat no. I8260) and immunoglobulin G (IgG) (cat no. I4506) from human serum (reagent grade, ∼95%) were purchased from Sigma-Aldrich (St. Louis, MO). Rabbit anti-SARS-CoV-2 S1 receptor binding domain (RBD) antibody and recombinant SARS-CoV-2 S1 subunit protein host cell receptor domain (RBD) were purchased from RayBiotech (cat. no. 230-30162). The Euroimmun SARS-CoV-2 ELISA IgA and IgG were purchased from Euroimmun, a PerkinElmer, Inc. Company, and authorized by the Food and Drug Administration. RT-PCR and antibody tests were performed by COVID-19 clinics in Ege University, Izmir. Laser patterning was performed by a CO_2 Universal Laser SystemsPLS6.75 laser with the laser spot diameter and wavelength of ∼150 and 10.6 μm, respectively. The commercial polyimide (PI) substrate (Kapton width: 12″) was purchased from Utech Products and used as the substrate. Previously optimized laser parameters were used. X-ray photoelectron spectroscopy (XPS) (Thermo Scientific) and scanning electron microscopy (SEM, Thermo Fischer Scientific Apreo S LoVac model, Oregon) were used for elemental analysis and morphological characterization, respectively. A PalmSens4 potentiostat (Palm Instruments, Houten, the Netherlands) was used for electrochemical measurements.

Preparation of LSG/AuNS Electrodes. For the fabrication of the electrodes, polyimide PI as a substrate was used for the fabrication of a three-electrode sensing system.[41] Following the LSG production, the working electrode (WE) surface was modified by electrochemical deposition using chronoamperometry, applying a constant potential of 0.9 V for 240 s in an electrolyte solution of 50 mM $HAuCl_4$ prepared in 0.5 M HCl. Finally, the gold-modified LSGs were cleaned with ultrapure water and the surface was dried with nitrogen gas.

Preparation of the Electrochemical Immunosensor. The gold surface was first modified with an aqueous cysteamine solution (1.1 mg/mL) and incubated for 1 h.[42] The surface then was washed with 0.05 M phosphate-buffered saline (PBS) to remove the excess unreacted cysteamine. Following the cysteamine immobilization, the electrode surface was covered with 8.0 μL of an EDC:NHS (50:50 mM) mixture for 5 h and then rinsed with 0.1 M PBS containing 0.1 M KCl to remove the unreacted EDC:NHS.[37,43] Next, 8.0 μL of the antibody (200 μg/mL prepared in 0.1 M PBS containing a 0.1 M KCl solution) was added to the working electrode surface

https://doi.org/10.1021/acs.analchem.1c01444
Anal. Chem. XXXX, XXX, XXX−XXX

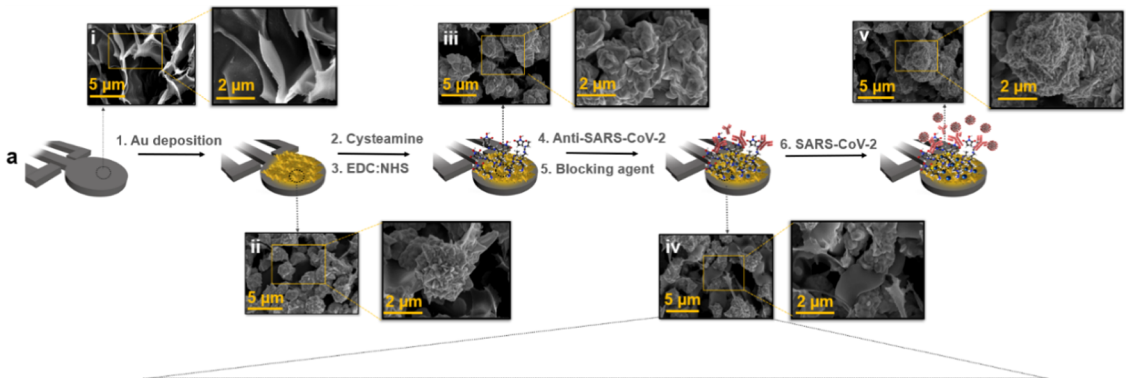

c	LSG	LSG/AuNS	LSG/AuNS/Cys	LSG/AuNS/Cys /EDC:NHS	LSG/AuNS/Cys/EDC:NHS/ Antibody
C1s	94.34	66.81	66.37	55.57	60.03
O1s	5.67	9.35	16.78	19.38	19.08
Au 4f	-	23.85	9.9	12.77	7.68
N1s	-	-	4.7	7.58	10.77

Figure 1. (a) Representation of each experimental step with scanning electron microscopy (SEM) images showing the morphology at high magnification (scale bar; 2 μm) and low magnification (scale bar; 5 μm); (b) X-ray photoelectron spectroscopy (XPS) data of LSG/AuNS/Cys/EDC:NHS/anti-SARS-CoV-2 showing O 1s, C 1s, N 1s, S 2p, and Au 4f7 high-resolution spectra; (c) XPS atomic percentages of C 1s, O 1s, S 2p, N 1s, and Au 4f after each preparation step of the immunosensor.

for 16 h incubation at 4 °C.[44] Electrodes were washed with 0.1 M PBS containing a 0.1 M KCl solution after the incubation of the antibody. As the last preparation step, 8.0 μL of 0.1 mg/mL BSA dissolved in 0.1 M PBS containing a 0.1 M KCl solution was placed onto the working electrode surface to block the unwanted active area.[45] The binder and antibody functionalization steps and different EDC:NHS and anti-SARS-CoV-2 S1 antibody concentrations were initially optimized prior to the sensing experiments. Finally, different concentrations of SARS-CoV-2 spike protein were tested to observe the antibody–analyte interaction.

Preparation of Serum Samples. We obtained 23 clinical serum samples from the Ege University Hospital (Izmir, Turkey). All patient samples were clinically identified as COVID-19 positive or negative by commercial RT-PCR, with the information describing that CT values above 35 indicate RT-PCR-negative and below 35 indicate RT-PCR-positive samples. Additionally, antibody and ELISA IgG and IgA tests were performed to assess the effectiveness of the gold-modified LSG sensors. Five of the patient samples gave negative RT-PCR results. The study was approved by the Ege University, Clinical Research Ethics Committee (20-8T/28). Blood serum was initially separated from plasma by centrifugation. Biosensing experiments were performed in the Central Research Test and Analysis Laboratory Application Center in Ege University (Turkey). The samples were used without any pretreatment prior to the incubation onto the LSG/AuNS electrode surface and electrochemical measurements. All dilutions were performed using 0.1 M PBS containing 0.1 M KCl at pH 7.4. Statistical analysis details are given in the Supporting Information (Tables S1–S4).

RESULTS AND DISCUSSION

Design and Characterization of the LSG/AuNS Immunosensor. Our design comprises three electrodes: AuNS-modified LSG working electrodes, an LSG counter electrode, and a reference electrode (RE). Pristine LSG does not possess enough functional attachments for necessary antibody immobilization. Figure 1a describes the preparation steps of the LSG/AuNS immunosensor. Initially, cysteamine was drop-cast on the working electrode surface, resulting in the presence of free ammonium groups attached to the surface through cysteamine. As the next step, cysteamine-modified LSG/AuNS was treated with EDC:NHS. This has an activation role for COOH groups present on the electrode surface for strong and rapid covalent coupling to amino-functionalized biorecognition elements. Therefore, the anti-spike protein antibody, known to be rich in carboxylic groups, was immobilized onto the surface, capturing free ammonium groups attached to the surface. Before proceeding with the spike protein detection, BSA was immobilized onto the surface to prevent nonspecific interactions and maintain the stability of the sensing performances in complex matrixes. As the final step, the protein present in the SARS-CoV-2 structure was formed on the surface. The highly porous three-dimensional (3D) structure of multilayer LSG is clearly seen in Figure 1a. After AuNS deposition onto the LSG working area, the formation of spiky flowery AuNS on the surface with high porosity was observed. After each modification step, the structural changes on the surface led to a slight increase in the polarity and relatively softer edges of the flowery shape of AuNS, given in Figure S1 at various magnifications. The XPS high-resolution spectra of the LSG/AuNS immunosensor (LSG/AuNS/Cys/EDC:NHS/anti-SARS-CoV-2/BSA),

https://doi.org/10.1021/acs.analchem.1c01444
Anal. Chem. XXXX, XXX, XXX−XXX

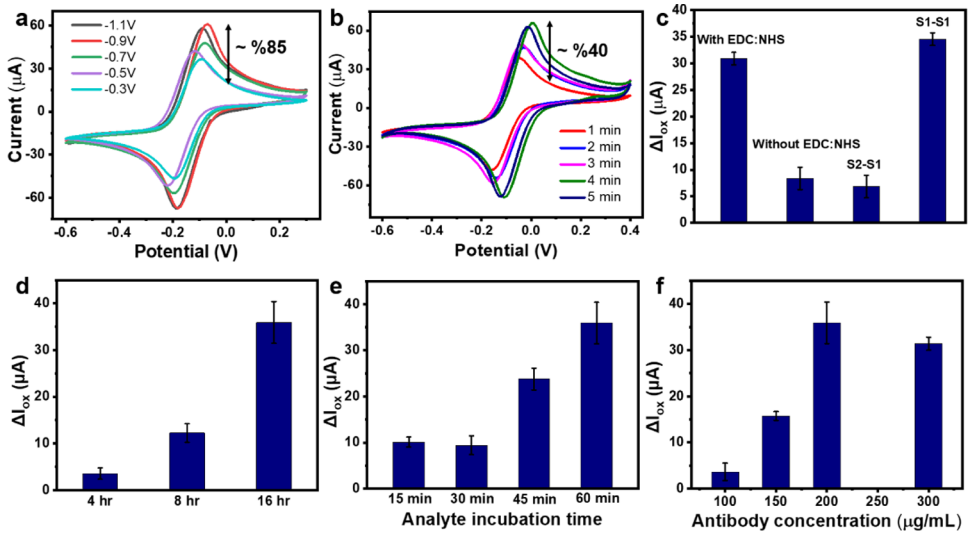

Figure 2. CV curves obtained for the LSG/AuNS sensor prepared using different (a) electrochemical depositions of the $HAuCl_4$ solution at different applied voltages in the range of −0.3 to −0.9 V and (b) electrodeposition times from 1 to 5 min; histograms showing ΔI_{ox} (the change in oxidation current) for (c) effect of EDC:NHS on SARS-CoV-2 binding and the effect of anti-SARS-CoV-2 S1 and S2 binding to the SARS-CoV-2 S1 protein; (d) effect of the incubation time of the antibody, (e) effect of the incubation time for the SARS-CoV-2 S1 protein; (f) effect of the anti-SARS-CoV-2 concentration on the electrochemical response of the LSG/AuNS biosensor. Error bars represent ±standard deviation (SD) and n = 3 samples. Measurements were performed in 5.0 mM $[Fe(CN)_6]^{3-/4-}$ containing 0.1 M PBS and 0.1 M KCl with a scan rate of 50 mV/s.

shown in Figure 1b, revealed the atomic presence of N and S in the working electrode surface by having C 1s, O 1s, Au 4f, N 1s, and S 2p photoelectrons. The XPS survey, high-resolution spectra, and atomic percentages found in the surface after each immobilization step are given in Figures S2−S7. The presence of N on the surface was supported by the atomic peak of N in energy-dispersive X-ray spectroscopy (EDX) data shown in Figure S8. Moreover, Figure 1c represents the atomic percentages of electrodes obtained by XPS after each modification step. The LSG/AuNS contains about 24% of Au 4f, proving the successful deposition of AuNS on the surface. Following the cysteamine deposition, around 4.4% of N 1s and 2.2% of S 2p were detected. The addition of EDC:NHS to the surface slightly increased the surface N 1s content, which could be attributed to the contribution from N atoms present in the EDC:NHS structure. Similarly, following the anti-SARS-CoV-2 incubation, the N 1s content kept increasing along with a slight increase in C 1s and O 1s contents.

Optimization of the Immunoassay. As a first step, the morphological difference between the bare LSG, LSG/AuNS, and gold screen-printed sensor was investigated. Figure S9 shows the scanning electron microscopy (SEM) images and energy-dispersive X-ray spectroscopy (EDX) identifying the elemental composition of the sensors. Additionally, the chronoamperometry parameters used for AuNS electrodeposition were optimized. SEM images showing different LSG/AuNS working electrode surfaces prepared using different electrodeposition voltages were compared to those of the bare LSG surface in Figure S10, indicating the effect of the applied voltage on the surface gold coverage. Among the different applied voltages between −0.3 and −0.9 V, Figure 2a shows that oxidation and reduction currents are stabilized after an ∼85% of increase in oxidation current for the immunosensor prepared at −0.9 V in a 50 mM solution of $HAuCl_4$. Additional CV measurements were performed to optimize the electrodeposition time for the AuNS modification. The electrodeposition time was tested in a range of 1−5 min, resulting in the highest electrochemical response for 4 min with an approximately ∼40% increase (Figure 2b). Another optimization test was carried out to study the effect of $HAuCl_4$ solution concentration on the performance of the LSG/AuNS sensor, by measuring 25, 50, 75, and 100 mM $HAuCl_4$ solutions. As can be seen in Figure S11, the highest electrochemical response was obtained from the measurements of the LSG/AuNS sensor prepared using 50 mM $HAuCl_4$. Though the coverage sustains at higher voltages and concentrations of a gold solution, electrocatalytic activity reduces due to the agglomeration, leading to a reduction of the current response. Therefore, 4 min and a 50 mM solution were selected for the further electrodeposition experiments.

The immobilization of the anti-SARS-CoV-2 S1 spike protein was also tested in the presence and absence of EDC:NHS. As shown in Figure 2c, the electrochemical response of the sensor was higher after EDC:NHS immobilization compared to the sensor response in the absence of EDC:NHS. Following EDC:NHS immobilization on top of the cysteamine layer resulted in an increase in proper ammonium groups to support the strong antibody binding to the surface. Another optimization test was performed by detecting the SARS-CoV-2 S1 spike protein by the LSG/AuNS immunosensor prepared by anti-SARS-CoV-2 S1 and anti-SARS-CoV-2 S2 separately, to identify the specific attachment between the antibody and analyte. Figure 2c shows that the S1 subunit of the SARS-CoV-2 spike protein has a stronger attraction toward the anti-SARS-CoV-2 S1 spike protein, resulting in a high drop in the oxidation current after the analyte immobilization onto the surface. The incubation time is another major factor affecting the LSG/AuNS immunosensor performance. After the identification of the antibody and EDC:NHS binder requirements, the antibody incubation time was optimized by varying it between 4 and 16 h, keeping the concentration of the antibody constant at 200 μg/mL (Figure 2d). The antibody amount was also optimized by

https://doi.org/10.1021/acs.analchem.1c01444
Anal. Chem. XXXX, XXX, XXX−XXX

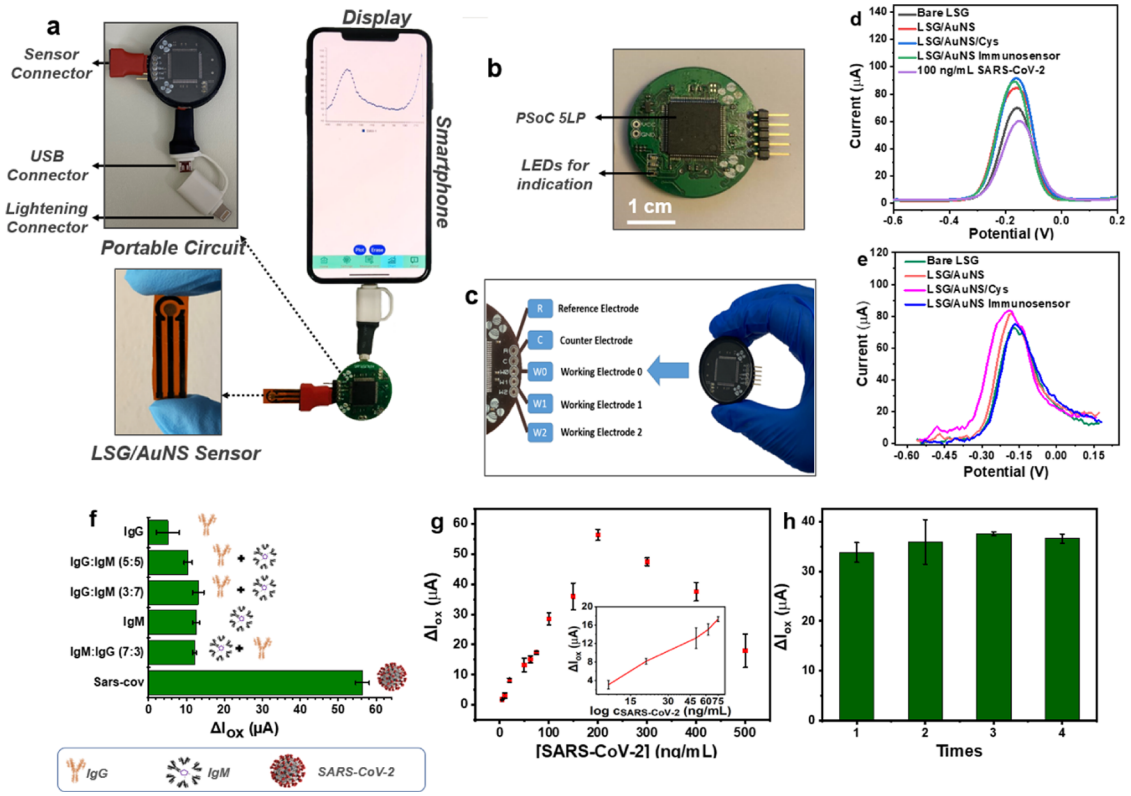

Figure 3. (a) Photo of the portable handmade POC potentiostat connected to a smartphone via a USB-C connection to record the signal using a customized KAUSTat software. (b) Close-up photo of the potentiostat device (scale bar: 1 cm). (c) Denotation of pinouts of KAUSTat; DPVs of the LSG\AuNS immunosensor presenting ΔI_{ox} (the change in oxidation current) after each experimental step and the measurement of 100 ng/mL SARS-CoV-2 spike protein by (d) PalmSens potentiostat and (e) portable handmade POC potentiostat. (f) Response of the LSG/AuNS immunosensor in the presence of SARS-CoV-2, IgM/IgG (7:3), IgM, IgG/IgM (3:7), IgG/IgM, and IgG (p value > 0.05). SARS-CoV-2 protein (150 ng/mL) and interfering proteins (immunoglobins, IgG and IgM) were used for the selectivity test. (g) Proposed LSG/AuNS immunosensor in response to different concentrations of the SARS-CoV-2 spike protein vs the LSG reference electrode. The inset shows the relationship between the ΔI_{ox} and the logarithm of the concentration of the S1 protein (log $C_{SARS\text{-}CoV\text{-}2}$). Histogram obtained for (h) repeatability study showed the test of the proposed sensor showing oxidation current responses of four different immunosensors prepared by the same procedure and 200 ng/mL SARS-CoV-2 protein. Error bars represent ±SD and n = 3 samples. Measurements were performed in 5.0 mM $[Fe(CN)_6]^{3-/4-}$ containing 0.1 M PBS and 0.1 M KCl with a scan rate of 50 mV/s.

incubating 100, 150, 200, and 300 μg/mL anti-SARS-CoV-2 S1 spike protein onto the LSG/AuNS immunosensor surface as shown in Figure 2f. As a result, the best oxidation current response was obtained from the LSG/AuNS immunosensor prepared by 16 h incubation of 200 μg/mL antibody. No significant variations were observed in the DPV response of the LSG/AuNS immunosensor prepared with antibody concentrations higher than 200 μg/mL. Finally, the SARS-CoV-2 S1 spike protein incubation time was optimized by testing the time range between 15 and 60 min with the same concentration of the S1 spike protein, resulting in the best current response obtained from the DPV of 60 min analyte incubation (Figure 2e). Thus, electrodeposition of gold was performed at −0.9 V for 4 min by applying a 50 mM gold chloride solution. Furthermore, the spike protein was incubated for 1 h following 16 h incubation of 200 μg/mL antibody for further experiments.

Integration of the LSG/AuNS Electrode into a Point-of-Care Device. We developed a second-generation custom-made POC electrochemical analyzer (KAUSTat), which was used as a proof of concept.[46] KAUSTat is a reconfigurable multimeasurement polypotentiostat device for multichannel electrochemical sensors, consisting of built-in memory, a battery, Bluetooth, a mini-USB connector, a slot for an SD card, and a connectable add-on device, enabling multiple amperometric and voltammetric measurements. Moreover, the device has a dual connector, enabling KAUSTat to be connected to a smartphone with a micro-USB port. KAUSTat connects directly to mobile application software and the phone battery.

Figure S12 shows the details of the operation system of the POC device connected to a specifically designed mobile application software. A photograph of the LSG/AuNS immunosensor, the components of the POC device, smartphone connection, a portable circuit, and a sensor integration unit of the device is demonstrated in Figure 3a. The size comparison and five pinouts of KAUSTat for three working electrodes (WE), one reference electrode (RE), and one counter electrode (CE) are presented in Figure 3b,c. The block diagram in Figure S13 shows the input/output peripherals and the representation of KAUSTat used as an add-on and a standalone watchlike device.

Analytical Features of SARS-CoV-2 Detection. Each modification step was validated by electrochemical measurements under the optimized conditions. Figure 3d shows the DPV signals for bare LSG, LSG/AuNS, LSG/AuNS/Cys, LSG/AuNS/Cys/EDC:NHS/anti-SARS-CoV-2/BSA, and LSG/AuNS/Cys/EDC:NHS/anti-SARS-CoV-2/BSA/SARS-

https://doi.org/10.1021/acs.analchem.1c01444
Anal. Chem. XXXX, XXX, XXX−XXX

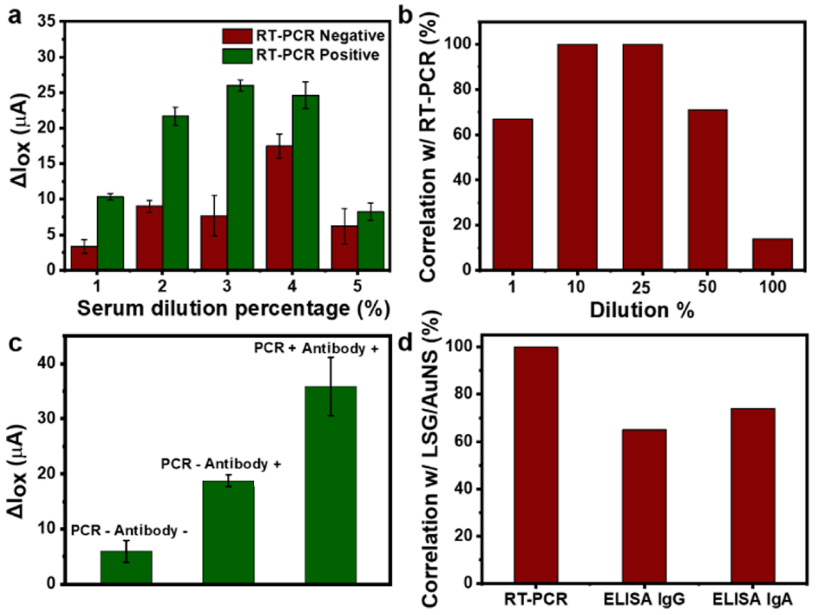

Figure 4. Histograms showing (a) ΔI_{ox} (the change in oxidation current) between RT-PCR-positive and -negative patient samples for each serum dilution percentage; (b) correlation between LSG/AuNS sensor and RT-PCR results for each dilution percentage of 23 patient serum samples; (c) ΔI_{ox} corresponding to different combinations of PCR and antibody test results; (d) correlation between LSG/AuNS sensor and RT-PCR, ELISA IgG, and IgA test results of 23 patient serum samples. Error bars represent ±SD and n = 3 samples. Measurements were performed in 5.0 mM $[Fe(CN)_6]^{3-/4-}$ containing 0.1 M PBS and 0.1 M KCl with a scan rate of 50 mV/s.

CoV-2 S1 protein. The sensor showed a significant increase in the oxidation current intensity after the electrodeposition of AuNS onto the LSG electrode. This current increase is attributed to the high conductivity due to the high surface area and excellent catalytic activity of AuNS, eventually leading to a better electron mobility at the electrode−electrolyte interface.

Moreover, the increase in the current value after cysteamine deposition can be related to the presence of polarizable ammonium groups on the electrode surface, strongly drawn to the negatively charged redox ions present at the electrolyte interface to ease the load transfer. Finally, due to the bulky structure resulting from the antibody−analyte binding, the electron transfer process on the surface was hindered, leading to a current decrease in DPV peaks. Figure 3d,e compares the DPV response of the LSG/AuNS immunosensor measured by the commercially available PalmSens electrochemical workstation and KAUSTat device. Despite the slight sensitivity difference, KAUSTat is able to identify each experimental step and the presence of the SARS-CoV-2 spike protein. Thus, the results prove that KAUSTat has a great potential as an alternative measuring system, compared to the widely used commercially available PalmSens electrochemical detection system.

A calibration plot is shown in Figure 3g, demonstrating the relation between SARS-CoV-2 S1 spike protein concentration (ng/mL) and oxidation current difference between antibody−analyte attachments (μA).

The concentration range of 5.0−500 ng/mL SARS-CoV-2 S1 spike protein was tested, and following an increase in the oxidation current change, saturation in response was observed due to the increase in the concentration of the analyte. As shown in Figure 3g inset, a linear logarithmic relationship was obtained in the range of 10−75 ng/mL analyte. The limit of detection (LOD) was calculated to be 2.9 ng/mL by defining log $C_{SARS\text{-}CoV\text{-}2}$ equivalent to the average ΔI_{ox} (the change in oxidation current) of the blank plus three times its standard deviation and using the following regression equation: ΔI_{ox} = 14.60 log C −11.27 with a correlation coefficient of 0.996. The electrochemical response was increased with the increase in concentration. Reproducibility was examined to confirm the reliability of the proposed immunosensor by preparing four different sensors based on the same preparation method, incubating with 200 ng/mL SARS-CoV-2 spike protein and measuring each sensor three times (Figure 3h). The variation in oxidation current response of four different immunosensors was found as 4.5% for the immunosensors, proving that our procedure can be considered as reliable.

Immunoglobins, IgG and IgM, glycoproteins produced by specific immune cells as the response to virus exposure, were selected as potential interferents for the selectivity test. Figure 3f shows the oxidation current change in DPV following IgG, IgM, and specific SARS-CoV-2 S1 spike protein incubation onto the LSG/AuNS immunosensor. Results were validated statistically, proving that there is a significant difference between the oxidation current values (p value: 8.75 × 10^{-13} < 0.05). The current response observed by other protein biomarkers, IgG and IgM, is related to the nonspecific binding of interfering substances, causing an oxidation current difference signal in DPV. However, an approximately 40% current difference was observed in the DPV signal between the actual target and the interferences due to the selective capturing, which proves that the proposed sensing system is selective for the SARS-CoV-2 S1 spike protein. In addition, histograms obtained for the mixtures of the interferents with different ratios (v/v) are presented in Figure S14.

The oxidation current signals of SARS-CoV-2 S1 spike protein, IgG, and IgM mixtures with different ratios were observed as 114, 107, 118, and 117% for SARS-CoV-2/IgM (2:1), SARS-CoV-2/IgG (2:1), SARS-CoV-2/IgM (4:1), and SARS-CoV-2/IgG (4:1), respectively, by considering 100% as SARS-CoV-2 response. Results were validated statistically, proving that there is no statistically significant difference

https://doi.org/10.1021/acs.analchem.1c01444
Anal. Chem. XXXX, XXX, XXX−XXX

Table 1. Serum Samples (with 25% Dilution) Analyzed Using the LSG/AuNS Biosensing System and RT-PCR, ELISA IgG, ELISA IgA, and Antibody Testing

sample	$\Delta I_{average}$ (A)	RSD (%)	proposed system[a]	RT-PCR[b]	ELISA IgG[c]	ELISA IgA[c]	antibody[b]
patient #1	0.027	3.08	+	+	+	+	na
patient #2	0.025	3.24	+	+	−	−	na
patient #3	0.024	2.94	+	+	+	+	na
patient #4	0.025	12	+	+	+	+	na
patient #5	0.024	16.4	+	+	−	+	na
patient #6	0.021	1.78	+	+	−	−	na
patient #7	0.024	5.43	+	+	−	−	na
patient #8	0.024	9.47	+	+	−	−	na
patient #9	0.023	1.82	+	+	+	+	na
patient #10	0.029	2.53	+	+	−	−	na
patient #11	0.019	6.11	+	+	−	+	na
patient #12	0.019	9.32	+	+	−	−	na
patient #13	0.023	26.3	+	+	na	na	+
patient #14	0.026	1.13	+	+	+	+	+
patient #15	0.036	14.8	+	+	+	+	+
patient #16	0.028	8.80	+	+	+	+	+
patient #17	0.036	7.20	+	+	+	+	+
patient #18	0.008	−	−	−	na	na	−
patient #19	0.008	−	−	−	−	−	−
patient #20	0.015	−	−	−	−	−	−
patient #21	0.006	−	−	−	−	−	−
patient #22	0.01	−	−	−	−	−	−
patient #23	0.006	−	−	−	na	na	+

[a](+) and (−) signs represent positive and negative tested patients, respectively. [b]RT-PCR and antibody tests were performed by COVID-19 clinics in Ege University (Izmir/Turkey). [c]The commercial SARS-COV-2 ELISA IgA and IgG were purchased from Euroimmun, a PerkinElmer, Inc. Company, and authorized for emergency use by the Food and Drug Administration (FDA).

between the oxidation current values regardless of the interferent additions to the spike protein (p value: 0.62 > 0.05). Therefore, it can be said that the designed platform recognizes the SARS-CoV-2 specific protein selectively among the other protein biomarkers.

Effect of Scan Rate and Flexibility Test. Pictures of the device during the bending process are presented in Figure S15a. The flexibility of the bare LSG, LSG/AuNS, and LSG/AuNS immunosensors was tested by bending the sensors for 1 min at ∼45 and ∼90°. It can be observed in Figure S15b that the oxidation current response remains unchanged after the bending of the sensors at ∼45 and ∼90°, proving that LSG electrodes are highly stable platforms for biosensing applications. Also, the measured sheet resistance of graphene multilayers is given as a function of bending duration (Figure S15c).

The scan rate effect was tested for the bare LSG and LSG/AuNS sensors, varying the scan rate from 40 to 140 mV/s. CV curves corresponding to the scan rate study of the sensors are presented with the calibration data in Figure S15d,e. The active surface area of the LSG/AuNS sensor was found to be 0.082 cm^2, greater than the active surface area of the LSG bare electrode, 0.057 cm^2. The active surface area is enhanced due to the excellent electrocatalytic activity of the AuNS-modified LSG working electrode. Therefore, the LSG/AuNS sensing system has a good potential for developing highly sensitive electrochemical immunoassays.

Determination of SARS-CoV-2 in Clinical Samples. The proposed sensor was validated using clinical serum samples, tested by RT-PCR, ELISA IgG, ELISA IgA, and IgG/IgM antibody testing. We measured the DPV of both RT-PCR-positive and -negative blood serum samples under the optimum conditions by replacing the spike incubation with clinical samples. The oxidation current difference between RT-PCR-positive and -negative patient samples for each serum dilution percentage (0, 1.0, 10, 25, and 50%) was studied to optimize the proper serum concentration for further measurements, as given in Tables S5−S9. A significant current reduction of the DPV signal was observed for the majority of both RT-PCR-positive and -negative samples, shown in Figures 4a and S16. This can be explained by the possible cross-reactivity in the serum samples. It should be noted that we did not need further filtration or centrifugation of the serum samples prior to the measurement since proteins or other substances in the serum samples could not be removed without affecting the virus concentration. The mean value (n = 3) with the corresponding standard deviation was considered for each measurement.

The correlation between LSG/AuNS sensor and RT-PCR results for each dilution percentage of serum samples in Figure 4b indicates that current measurements of 10 and 25% diluted samples yield the best correlation with the RT-PCR test.

Oxidation current values corresponding to RT-PCR-positive and -negative patient samples based on different serum concentrations were statistically validated by the two-factor analysis of variance (ANOVA) test with replication. The p value of RT-PCR-positive serum samples was found to be relatively low (p: 1.96×10^{-14} <0.05), proving that the current response of RT-PCR-positive serum samples at different dilution concentrations are significantly different. On the other hand, the p value of RT-PCR-negative serum samples was found to be relatively high (p: 0.42 > 0.05), proving that there is no significant difference between the current response of RT-PCR-negative serum samples at different concentrations.

https://doi.org/10.1021/acs.analchem.1c01444
Anal. Chem. XXXX, XXX, XXX−XXX

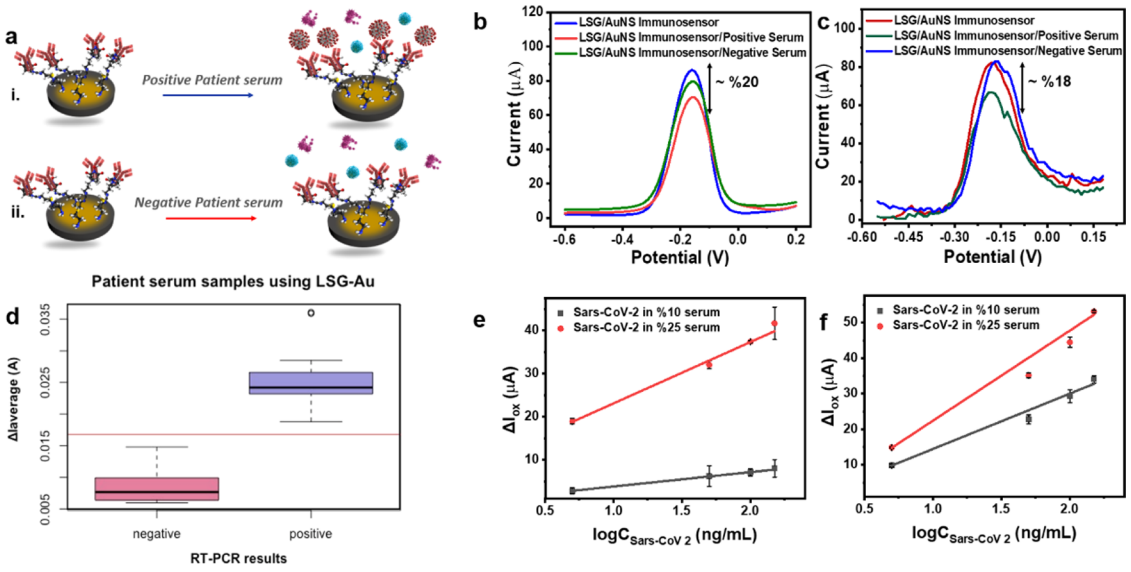

Figure 5. (a) Representation of SARS-CoV-2 detection in human blood serum. DPVs for LSG/AuNS/Cys/EDC:NHS/anti-SARS-CoV-2/BSA, LSG/AuNS/Cys/EDC:NHS/anti-SARS-CoV-2/BSA/positive serum, and LSG/AuNS/Cys/EDC:NHS/anti-SARS-CoV-2/BSA/negative serum obtained by (b) PalmSens potentiostat and (c) portable handmade POC potentiostat. (d) Boxplot analysis of the averaged peak current obtained from 23 patient samples using LSG/AuNS; the red line marks the threshold of classification in which all signals above 0.0168 A were classified as positive and confirmed by RT-PCR. Linear plots of ΔI_{ox} (oxidation current change) vs SARS-CoV-2 concentrations obtained from LSG/AuNS in (e) 10 and 25% of COVID-19-positive blood serum and (f) 10 and 25% in COVID-19-negative blood serum. Error bars represent ±SD and $n = 3$ samples. Measurements were performed in 5.0 mM $[Fe(CN)_6]^{3-/4-}$ containing 0.1 M PBS and 0.1 M KCl with a scan rate of 50 mV/s.

Thus, we have found that the highest and lowest current reductions were achieved with 25% dilution of RT-PCR-positive and -negative blood serum samples, respectively, with the minimum interference effect. In the case of the RT-PCR-positive serum samples, the current reduction was observed to be larger, while a relatively small current reduction was observed for the RT-PCR-negative patients.

Table 1 summarizes the obtained patient samples by presenting the obtained oxidation current reduction for each patient sample. The results of our LSG/AuNS immunosensor were validated by performing ELISA IgG/IgA tests and RT-PCR and IgG/IgM antibody tests performed by COVID-19 clinics. Three repetitions were performed for each patient, and detailed data is presented in Table S9. The difference between oxidation current values of the LSG/AuNS immunosensor after both antibody and patient serum immobilization were statistically verified by the *t*-test with paired two sample for means. For the positive samples, the t_{stat} value was found to be larger than $t_{critical}$, leading to a small $p_{two\text{-}tail}$ value (p: 0.001 < 0.05), proving that the oxidation current values measured after antibody immobilization are significantly different from the current values after serum immobilization. Oppositely, for the negative samples, the t_{stat} value was found to be smaller than $t_{critical}$, leading to a large $p_{two\text{-}tail}$ value (p: 0.3 > 0.05), proving that there is no significant difference between the oxidation current values measured after antibody immobilization and after serum immobilization. Moreover, the DPV oxidation current responses of the LSG/AuNS immunosensor to different combinations of antibody/RT-PCR-positive and -negative patient samples were recorded for comparison purposes (Figure 4). The oxidation current difference corresponding to PCR and antibody test result combinations are presented in Figures 4c and S17. We observed a slight current increase following a nonspecific binding for PCR (−) antibody (+) patient samples. However, the current change increased around 2-fold for PCR (+) antibody (+) patient samples compared to PCR (−) antibody (+) patient samples; therefore, it is more noticeable. We tested the correlation between our proposed test and commercially available RT-PCR and ELISA IgG and IgA test results, and our test yielded the best agreement with the RT-PCR test. Moreover, ELISA IgG and IgA tests were found, respectively, in 65 and 74% agreement with the LSG/AuNS immunosensor (Figure 4d). Therefore, our approach is most compatible with the RT-PCR tests among the commercial validation test kits. Taking into account that ELISA tests have a high possibility of leading to false-positive or -negative results due to the effect of insufficient washing, cross-reactivity from preexisting antibodies, or other possible interferences in the presence of the low viral load, our results are considered as very satisfactory.

Figure 5a shows the detection mechanism of the SARS-CoV-2 S1 spike protein in blood serum. DPVs of the LSG/AuNS immunosensor measured before and after patient serum incubation by a PalmSens potentiostat and our KAUSTat device are compared in Figure 5b,c, respectively. Based on the current response of the patient serum samples, we took a statistical approach to identify a threshold value. The threshold was determined by the boxplot analysis of the averaged peak current obtained from 23 patient samples using LSG/AuNS, presented in Figure 5d. The red line marks the threshold of classification in which all signals above 0.0168 A were classified as positive and confirmed by the RT-PCR test. Moreover, the analytical characterization of RT-PCR-positive and -negative serum samples by the LSG/AuNS immunosensor was performed by the standard addition method. Linear plots of the oxidation current difference of the LSG/AuNS immunoassay versus SARS-CoV-2 S1 spike protein additions in the presence of 10 and 25% diluted positive and negative serum are presented in Figure 5e,f. The LODs were calculated as ~3.0 and ~8.0 ng/mL in 10 and 25% diluted RT-PCR-

https://doi.org/10.1021/acs.analchem.1c01444
Anal. Chem. XXXX, XXX, XXX−XXX

negative serum, respectively. The results show that LOD values for 10 and 25% diluted RT-PCR-positive serum were increased to ~16 and ~10 ng/mL, respectively, proving the effect of the real SARS-CoV-2 S1 spike protein in positive blood serum. These LODs were calculated from the signal-to-noise ratio ($S/N = 3$) at a 95% confidence interval.

Table S10 summarizes the analytical features and detection methods of various biosensor platforms developed for SARS-CoV-2 detection. Compared to previously developed COVID-19 diagnostic tests shown in the table, our LSG/AuNS immunosensor provides fast results with the requirement of 1 h incubation and a practical POC diagnosis with satisfactory analytical features. We believe that this portable POC diagnostic platform provides a highly accessible screening in both field and personal applications.

CONCLUSIONS

We describe a smart antibody sensor based on electrodeposition of AuNS on LSG electrodes for SARS-CoV-2 detection with a calculated LOD of 2.9 ng/mL. The detection system was successfully applied to 23 blood serum samples of COVID-19 patients for clinical validation. We tested the correlation between our proposed test and commercially available test results, and our test yielded the best agreement with the RT-PCR test. The results show that the proposed sensor has the possibility to be an alternative detection method with a convenient detection time. The integration of the sensor into a POC device provides ease of use in SARS-CoV-2 detection from blood serum samples. Though further improvements are required for LSG/AuNS electrodes to develop fully optimized POC diagnostic tools, the proposed sensing system offers a good and stable alternative platform for future applications. With further optimizations and modifications, detection of SARS-CoV-2 in other samples such as nasopharyngeal swab specimens will be part of our ongoing research in the future.

ASSOCIATED CONTENT

Supporting Information

The Supporting Information is available free of charge at https://pubs.acs.org/doi/10.1021/acs.analchem.1c01444.

Laser scribing; electrochemical measurements; statistical analysis; characterizations; KausTat; analytical features; effect of scan rate; and real serum standard addition measurements (PDF)

AUTHOR INFORMATION

Corresponding Authors

Khaled N. Salama − *Sensors Lab, Advanced Membranes and Porous Materials Center, Computer, Electrical and Mathematical Science and Engineering Division, King Abdullah University of Science and Technology (KAUST), Thuwal 23955-6900, Saudi Arabia;* orcid.org/0000-0001-7742-1282; Email: khaled.salama@kaust.edu.sa

Suna Timur − *Central Research Test and Analysis Laboratory Application and Research Center, Ege University, 35100 Bornova, Izmir, Turkey; Department of Biochemistry, Faculty of Science, Ege University, 35100 Bornova, Izmir, Turkey;* orcid.org/0000-0002-3129-8298; Email: suna.timur@ege.edu.tr

Authors

Tutku Beduk − *Sensors Lab, Advanced Membranes and Porous Materials Center, Computer, Electrical and Mathematical Science and Engineering Division, King Abdullah University of Science and Technology (KAUST), Thuwal 23955-6900, Saudi Arabia;* orcid.org/0000-0001-7365-6404

Duygu Beduk − *Central Research Test and Analysis Laboratory Application and Research Center, Ege University, 35100 Bornova, Izmir, Turkey*

José Ilton de Oliveira Filho − *Sensors Lab, Advanced Membranes and Porous Materials Center, Computer, Electrical and Mathematical Science and Engineering Division, King Abdullah University of Science and Technology (KAUST), Thuwal 23955-6900, Saudi Arabia*

Figen Zihnioglu − *Department of Biochemistry, Faculty of Science, Ege University, 35100 Bornova, Izmir, Turkey*

Candan Cicek − *Department of Medical Microbiology, Faculty of Medicine, Ege University, 35100 Bornova, Izmir, Turkey*

Ruchan Sertoz − *Department of Medical Microbiology, Faculty of Medicine, Ege University, 35100 Bornova, Izmir, Turkey*

Bilgin Arda − *Department of Infectious Diseases and Clinical Microbiology, Faculty of Medicine, Ege University, 35100 Bornova, Izmir, Turkey*

Tuncay Goksel − *Department of Pulmonary Medicine, Faculty of Medicine, Ege University, 35100 Bornova, Izmir, Turkey; EGESAM-Ege University Translational Pulmonary Research Center, 35100 Bornova, Izmir, Turkey*

Kutsal Turhan − *Department of Thoracic Surgery, Faculty of Medicine, Ege University, 35100 Bornova, Izmir, Turkey*

Complete contact information is available at: https://pubs.acs.org/10.1021/acs.analchem.1c01444

Author Contributions

S.T., K.N.S., K.T., T.G., B.A., R.S., C.C., and F.Z. conceived and conceptualized the study, provided resources, and acquired funding. T.B. and D.B. performed the characterization and electrochemical measurements. J.I.O.F. developed the potentiostat device and wrote the software for the POC measurements. T.B and D.B. wrote the manuscript with the supervision of S.T. and K.N.S.

Notes

The authors declare no competing financial interest.

ACKNOWLEDGMENTS

The authors would like to express their acknowledgments to the financial support from Ege University, Research Foundation (Project No. TOA-2020-21862) and King Abdullah University of Science and Technology (KAUST), Saudi Arabia.

REFERENCES

(1) Wu, F.; Zhao, S.; Yu, B.; Chen, Y.-M.; Wang, W.; Song, Z.-G.; Hu, Y.; Tao, Z.-W.; Tian, J.-H.; Pei, Y.-Y.; Yuan, M.-L.; Zhang, Y.-L.; Dai, F.-H.; Liu, Y.; Wang, Q.-M.; Zheng, J.-J.; Xu, L.; Holmes, E. C.; Zhang, Y.-Z. *Nature* **2020**, *579*, 265−269.

(2) Wrapp, D.; Wang, N.; Corbett, K. S.; Goldsmith, J. A.; Hsieh, C.-L.; Abiona, O.; Graham, B. S.; McLellan, J. S. *Science* **2020**, *367*, 1260−1263.

(3) Pokhrel, P.; Hu, C.; Mao, H. *ACS Sens.* **2020**, *5*, 2283−2296.

(4) Walls, A. C.; Park, Y.-J.; Tortorici, M. A.; Wall, A.; McGuire, A. T.; Veesler, D. *Cell* **2020**, *181*, 281−292.e6.

(5) Han, Q.; Lin, Q.; Jin, S.; You, L. *J. Infect.* **2020**, *80*, 373−377.
(6) Feng, W.; Newbigging, A. M.; Le, C.; Pang, B.; Peng, H.; Cao, Y.; Wu, J.; Abbas, G.; Song, J.; Wang, D.-B.; Cui, M.; Tao, J.; Tyrrell, D. L.; Zhang, X.-E.; Zhang, H.; Le, X. C. *Anal. Chem.* **2020**, *92*, 10196−10209.
(7) Ter-Ovanesyan, D.; Gilboa, T.; Lazarovits, R.; Rosenthal, A.; Yu, X.; Li, J. Z.; Church, G. M.; Walt, D. R. *Anal. Chem.* **2021**, *93*, 5365−5370.
(8) Clemente, A.; Alba-Patiño, A.; Santopolo, G.; Rojo-Molinero, E.; Oliver, A.; Borges, M.; Aranda, M.; del Castillo, A.; de la Rica, R. *Anal. Chem.* **2021**, *93*, 5259−5266.
(9) Wang, C.; Yang, X.; Gu, B.; Liu, H.; Zhou, Z.; Shi, L.; Cheng, X.; Wang, S. *Anal. Chem.* **2020**, *92*, 15542−15549.
(10) Serrano, M. M.; Rodríguez, D. N.; Palop, N. T.; Arenas, R. O.; Córdoba, M. M.; Mochón, M. D. O.; Cardona, C. G. *J. Clin. Virol.* **2020**, *129*, 104529.
(11) Thompson, D.; Lei, Y. *Sens. Actuators Rep.* **2020**, *2*, No. 100017.
(12) Javalkote, V. S.; Kancharla, N.; Bhadra, B.; Shukla, M.; Soni, B.; Goodin, M.; Bandyopadhyay, A.; Dasgupta, S. *Methods* **2020**, DOI: 10.1016/j.ymeth.2020.10.003.
(13) Grant, B. D.; Anderson, C. E.; Williford, J. R.; Alonzo, L. F.; Glukhova, V. A.; Boyle, D. S.; Weigl, B. H.; Nichols, K. P. *Anal. Chem.* **2020**, *92*, 11305−11309.
(14) Yu, S.; Nimse, S. B.; Kim, J.; Song, K.-S.; Kim, T. *Anal. Chem.* **2020**, *92*, 14139−14144.
(15) Peeling, R. W.; Wedderburn, C. J.; Garcia, P. J.; Boeras, D.; Fongwen, N.; Nkengasong, J.; Sall, A.; Tanuri, A.; Heymann, D. L. Serology testing in the COVID-19 pandemic response.
(16) Zhao, H.; Liu, F.; Xie, W.; Zhou, T.-C.; OuYang, J.; Jin, L.; Li, H.; Zhao, C.-Y.; Zhang, L.; Wei, J.; Zhang, Y.-P.; Li, C.-P. *Sens. Actuators, B* **2021**, *327*, No. 128899.
(17) Xiao, A. T.; Tong, Y. X.; Gao, C.; Zhu, L.; Zhang, Y. J.; Zhang, S. J. J. oC. V. *J. Clin. Virol.* **2020**, *127*, No. 104346.
(18) Jin, Y.; Wang, M.; Zuo, Z.; Fan, C.; Ye, F.; Cai, Z.; Wang, Y.; Cui, H.; Pan, K.; Xu, A. *Int. J. Infect. Dis.* **2020**, *94*, 49−52.
(19) Moulahoum, H.; Ghorbanizamani, F.; Zihnioglu, F.; Turhan, K.; Timur, S. *Talanta* **2021**, *222*, No. 121534.
(20) Sharafeldin, M.; Davis, J. J. *Anal. Chem.* **2021**, *93*, 184−197.
(21) Giovannini, G.; Haick, H.; Garoli, D. *ACS Sens.* **2021**, *6*, 1408−1417.
(22) Shan, B.; Broza, Y. Y.; Li, W.; Wang, Y.; Wu, S.; Liu, Z.; Wang, J.; Gui, S.; Wang, L.; Zhang, Z.; Liu, W.; Zhou, S.; Jin, W.; Zhang, Q.; Hu, D.; Lin, L.; Zhang, Q.; Li, W.; Wang, J.; Liu, H.; et al. *ACS Nano* **2020**, *14*, 12125−12132.
(23) Fabiani, L.; Saroglia, M.; Galatà, G.; De Santis, R.; Fillo, S.; Luca, V.; Faggioni, G.; D'Amore, N.; Regalbuto, E.; Salvatori, P.; Terova, G.; Moscone, D.; Lista, F.; Arduini, F. *Biosens. Bioelectron.* **2021**, *171*, No. 112686.
(24) Yakoh, A.; Pimpitak, U.; Rengpipat, S.; Hirankarn, N.; Chailapakul, O.; Chaiyo, S. *Biosens. Bioelectron.* **2021**, *176*, No. 112912.
(25) Seo, G.; Lee, G.; Kim, M. J.; Baek, S.-H.; Choi, M.; Ku, K. B.; Lee, C.-S.; Jun, S.; Park, D.; Kim, H. G.; Kim, S.-J.; Lee, J.-O.; Kim, B. T.; Park, E. C.; Kim, S. I. *ACS Nano* **2020**, *14*, 5135−5142.
(26) Tian, H.; Chen, H.-Y.; Ren, T.-L.; Li, C.; Xue, Q.-T.; Mohammad, M. A.; Wu, C.; Yang, Y.; Wong, H. S. P. *Nano Lett.* **2014**, *14*, 3214−3219.
(27) Lahcen, A. A.; Rauf, S.; Beduk, T.; Durmus, C.; Aljedaibi, A.; Timur, S.; Alshareef, H. N.; Amine, A.; Wolfbeis, O. S.; Salama, K. N. *Biosens. Bioelectron.* **2020**, *168*, No. 112565.
(28) Ahmad, R.; Wolfbeis, O. S.; Hahn, Y.-B.; Alshareef, H. N.; Torsi, L.; Salama, K. N. *Mater. Today Commun.* **2018**, *17*, 289−321.
(29) Ghanam, A.; Lahcen, A. A.; Beduk, T.; Alshareef, H. N.; Amine, A.; Salama, K. N. *Biosens. Bioelectron.* **2020**, *168*, No. 112509.
(30) Palmieri, V.; Papi, M. *Nano Today* **2020**, *33*, No. 100883.
(31) Ziem, B.; Azab, W.; Gholami, M. F.; Rabe, J. P.; Osterrieder, N.; Haag, R. *Nanoscale* **2017**, *9*, 3774−3783.
(32) Li, X.; Cai, W.; An, J.; Kim, S.; Nah, J.; Yang, D.; Piner, R.; Velamakanni, A.; Jung, I.; Tutuc, E.; Banerjee, S. K.; Colombo, L.; Ruoff, R. S. *Science* **2009**, *324*, 1312−1314.
(33) Georgakilas, V.; Tiwari, J. N.; Kemp, K. C.; Perman, J. A.; Bourlinos, A. B.; Kim, K. S.; Zboril, R. *Chem. Rev.* **2016**, *116*, 5464−5519.
(34) Soares, R. R. A.; Hjort, R. G.; Pola, C. C.; Parate, K.; Reis, E. L.; Soares, N. F. F.; McLamore, E. S.; Claussen, J. C.; Gomes, C. L. *ACS Sens.* **2020**, *5*, 1900−1911.
(35) Lei, Y.; Alshareef, A. H.; Zhao, W.; Inal, S. *ACS Appl. Nano Mater.* **2020**, *3*, 1166−1174.
(36) Nayak, P.; Kurra, N.; Xia, C.; Alshareef, H. N. *Adv. Electron. Mater.* **2016**, *2*, No. 1600185.
(37) Fenzl, C.; Nayak, P.; Hirsch, T.; Wolfbeis, O. S.; Alshareef, H. N.; Baeumner, A. J. *ACS Sens.* **2017**, *2*, 616−620.
(38) Rauf, S.; Lahcen, A. A.; Aljedaibi, A.; Beduk, T.; Ilton de Oliveira Filho, J.; Salama, K. N. *Biosens. Bioelectron.* **2021**, *180*, No. 113116.
(39) Rauf, S.; Mani, V.; Lahcen, A. A.; Yuvaraja, S.; Beduk, T.; Salama, K. N. J. E. A. *Electrochim. Acta* **2021**, *386*, No. 138489.
(40) Hernández-Rodríguez, J. F.; Rojas, D.; Escarpa, A. *Anal. Chem.* **2021**, *93*, 167−183.
(41) Beduk, T.; Lahcen, A. A.; Tashkandi, N.; Salama, K. N. *Sens. Actuators, B* **2020**, *314*, No. 128026.
(42) Balaban, S.; Durmus, C.; Aydindogan, E.; Gumus, Z. P.; Timur, S. *Electroanalysis* **2020**, *32*, 128−134.
(43) Zahed, M. A.; Barman, S. C.; Das, P. S.; Sharifuzzaman, M.; Yoon, H. S.; Yoon, S. H.; Park, J. Y. *Biosens. Bioelectron.* **2020**, *160*, No. 112220.
(44) Barman, S. C.; Abu Zahed, M.; Sharifuzzaman, M.; Ko, S. G.; Yoon, H.; Nah, J. S.; Xuan, X.; Park, J. Y. *Adv. Funct. Mater.* **2020**, *30*, No. 1907297.
(45) D'Aurelio, R.; Chianella, I.; Goode, J. A.; Tothill, I. E. *Biosensors* **2020**, *10*, No. 22.
(46) Ahmad, R.; Surya, S. G.; Sales, J. B.; Mkaouar, H.; Catunda, S. Y. C.; Belfort, D. R.; Lei, Y.; Wang, Z. L.; Baeumner, A.; Wolfbeis, O. S. In *2019 IEEE SENSORS*, IEEE, 2019; pp 1−4.

https://doi.org/10.1021/acs.analchem.1c01444
Anal. Chem. XXXX, XXX, XXX−XXX